PERGAMON

Computers & Fluids 28 (1999) 41–61

computers & fluids

Disk-driven vortical flow structure in a cubical container

T.P. Chiang, W.H. Sheu, S.F. Tsai

Department of Naval Architecture and Ocean Engineering, National Taiwan University, 73 Chou-Shan Rd., Taipei, Taiwan

Received 17 April 1997; received in revised form 30 October 1997

Abstract

Our aim in conducting the numerical simulation of laminar flow in a cubical container is to explore into the flow structure subjected to a disk rotation on the roof of the container. To this end, we have applied the topology theory to analyze skin-friction lines or limiting streamlines to elucidate the kinematically possible vortical flow structure. For this study, four different Reynolds numbers in the range of Re = 500–2000 were considered, with emphasis on the case with Re = 1000. Revealed from the analysis is that the secondary flow structure emerges as a result of a plane disk rotating motion. The two-cell counter-rotating flow pattern in the plane perpendicular to the rotating disk is spatially varying due to the four corners present in the cubical container. We have also depicted the vortical flow structure in terms of vortex cores which provide more details about how mixing of the flow can be achieved through a simple plane disk rotation.

1. Introduction

The flow driven by a sliding block represents a domain of fluid mechanics which is of great academic and practical importance [1, 2]. Vortical flows driven by a rotating disk in a cylinder or rectangular container are often referred to in the processing industry. Geometric simplicity helps us to conduct analysis and helps provide a fundamental understanding of the rotating flow structure. Existing studies on such disk-driven flows are limited to flows in a cylindrical enclosure subjected to a rotating disk [3]. This confined flow is featured by a primary flow in the rotation direction and a secondary flow in the planes perpendicular to the rotation axis. While the secondary flow development in a rectangular container is critical to the mixing tank application and to chemical vapor deposition (CVD) in a quartz reactor, research into this problem is seldom seen in the literature. It is this lack of knowledge of the flow structure in the rectangular enclosure which motivated us to conduct this study with a view to filling the gap in our understanding. We address the effect of container corners on the developing secondary flows.

0045-7930/99/$ - see front matter
PII: S0045-7930(97)00065-0

Over the past 40 years, computers have increased in speed roughly by an order of magnitude per decade, making it possible to simulate large-scale Navier–Stokes flows which were previously intractable. With three-dimensional computations becoming more feasible, we are faced with analyzing a wealth of data from which detailed flow structure inferred from computations can be obtained. To put the data analysis in perspective, it is essential to apply a method which has a mathematically rigorous foundation. Use of this method is particularly needed to gain insight into the vortical flow structure. To achieve this goal, we have a choice of conducting topological studies on vector fields [4–6] or graphical visualizations of scalar helicity [7]. Our research effort is directed towards studying the influence of rotation-disk speeds on the topological structure of the flow. Classification of singular points on solid walls as well as in the core of the rectangular container has been accomplished. This helps to provide greater insight into the detailed primary and secondary flows which vary with the rotation speed or the Reynolds number.

This paper is organized as follows. The working equations and closure boundary conditions are given in Section 2. In Section 3, we provide a brief introduction to the segregated-type algorithm, which is chosen to iteratively compute the finite volume discretization equations. This is followed by a code validation study. To provide readers with physical details, we address in Section 4 use of limiting streamlines or skin-friction lines as the target vector fields. An analytic validation of the computer code is also included in the Result section. With the finite volume solutions thus obtained, we are able to conduct a topological study of the computed primitive velocity vectors in Section 4. This study provides insight into the structure of vortical flows driven by a rotating disk on the roof of the container.

2. Working equations

We consider in this paper the Navier–Stokes equations for velocity u and pressure p:

$$\frac{\partial}{\partial x_m}(u_m u_i) = -\frac{\partial p}{\partial x_i} + \frac{1}{Re}\frac{\partial^2 u_i}{\partial x_m \partial x_m}. \tag{1}$$

The above equations of motion are under the constraint condition of fluid incompressibility:

$$\frac{\partial u_i}{\partial x_i} = 0. \tag{2}$$

For this study, we concentrate to steady and laminar conditions. The Reynolds number Re is defined by choosing the maximum rotation speed of the disk (Rw) as the characteristic speed and the radius of the rotating disk (R) as the characteristic length. In this study, the pressure has been normalized by pR^2w^2 where w denotes the angular velocity of the disk.

The rationale behind adopting the velocity–pressure formulation is that it provides closure boundary conditions [8]. Referring to Fig. 1, no-slip boundary conditions for velocities u_i are specified everywhere except at the upper wall, where a disk of radius 1 rotates with a constant value of ω which is referred to as the disk angular speed. No pressure boundary condition is

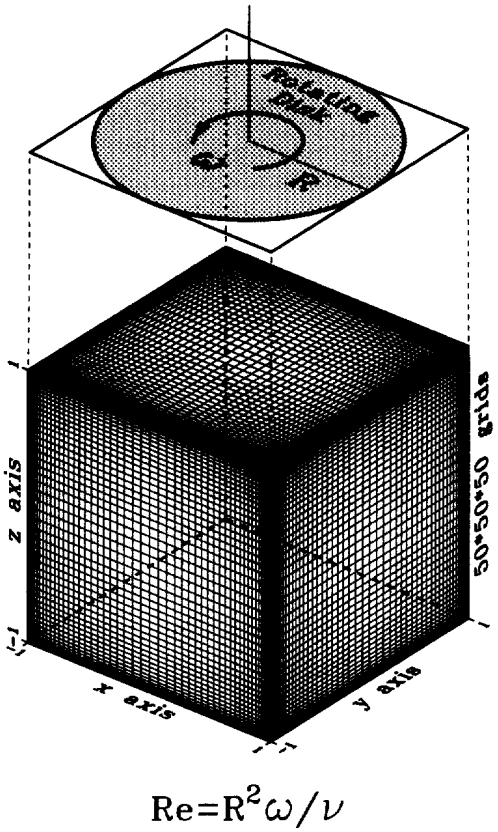

Fig. 1. Description of the investigated rotating disk-driven cavity problem and the non-uniform grid distribution ($50 \times 50 \times 50$) on the bounding surfaces.

permitted at the boundary where velocities are specified; otherwise, the investigated elliptic system will be overdetermined [8].

3. Finite volume method and solution algorithm

We then discretize working equations cast in the primitive–variable form and transform them into algebraic counterparts that are amenable to computer simulation. In collocating the grids, the divergence-free constraint condition is the main cause of even–odd pressure oscillations. Schemes of Chorin [9], Strikwerda [10], Rhie and Chow [11], Abdallah [12], and Schneider and Raw [13] are methods of choice to resolve instabilities of this type for incompressible flow analyses at non-staggered grids. For this study, we advocate use of staggered grids of Harlow and Welch [14], while collocating grids facilitate the programming. The reason for advocating staggered grids is that we can avoid specifying pressure boundary conditions in the use of projection–step methods. In addition, use of staggered grids fits the

nature of finite volume method employed here. In each cell, the representative field variable is assumed to be constant and is physically placed in the cell centroid. Finite volume integration of the associated working equation is made. Velocities are staggered with respect to pressure to prevent the spurious oscillations in the pressure solution.

In the mixed (coupled) formulation, the absence of pressure in the continuity equation tend to increase the condition number of the discrete system and, thus, complicate the computation. The accompanying zero diagonals in the matrix equation are also harmful to Gaussian elimination-like solution solvers. In order to permit large-scale computations, we were prompted to apply the SIMPLE segregated solution algorithm [15]. Instead of analyzing the working equations in a strongly coupled fashion, SIMPLE solves a Poisson equation for the pressure difference as a means to incorporate the incompressibility constraint into the formulation. Segregated solution algorithm outperforms the mixed formulation because of the save in the overhead needed to store the encountered matrix equations.

As grid lines increasingly deviate from streamlines, false diffusion errors tend to overspread the flow physics. The deterioration of the prediction accuracy is particularly severe in high Reynolds number circumstances. For this reason, the QUICK scheme of Leonard [16] is thus favorable to approximate advective fluxes in a non-uniformly discretized domain. Since discretization errors of metric tensors in the curvilinear coordinate transformation may be considerable and are difficult to resolve for problems whose configurations involve an abrupt change in the curvilinear lines, we conduct analysis simply in a Cartesian coordinate system. This helps retain the true nature of the flow.

We have benchmarked the computer code employed here by taking the analytic velocity vector $u(x,y,z,t = 0)$, as given in the problem of Ethier and Steinman [17], as the specified boundary velocities. In this study, solutions computed at the finest grid ($h = 1/27$) are regarded as reference values for conducting the rate of convergence test. According to our previous work [18], the rates of convergence for velocities and pressure are plotted in Fig. 2. The success in validating the analysis code provides us with strong confidence to study the driven cavity flow subjected to a rotating disk.

4. Results and discussions

4.1. Problem description

The disk-container assembly is shown schematically in Fig. 1. On the roof of the cavity, a disk of radius 1 is mounted coaxially with the centroid of the cubical cavity, which has a length of 2. This disk rotates constantly with an angular velocity ω, driving an initially resting liquid fluid and thereby resulting in a vortical flow. For this study, we address the effect of the rotation speed, or Reynolds number as defined in Section 2, of the disk on the established vortical flow structure. We also explore into the kinematic aspect of the primary vortical flow and the secondary flow. The Reynolds numbers considered in this study are 500, 1000, 1500 and 2000.

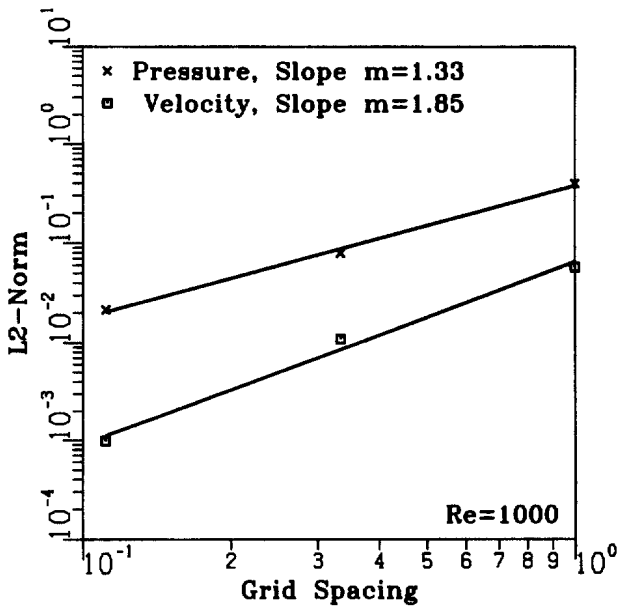

Fig. 2. Rates of convergence for velocity magnitude $(u^2+v^2+w^2)^{1/2}$ as well as pressure.

4.2. Disk-driven vortical flows

Prior to the discussion of computed solutions, it is instructive to perform the grid independence test for the target problem with $Re = 1000$. With mesh being continuously refined, we have plotted in Fig. 3 the mid-sectional u,v velocities at $z = 0.9$, 0.0, and -0.9 planes and $w(0., 0., z)$. As this figure shows, we demonstrate the applicability of the finite volume method to numerical simulation of the disk-driven flow problem. In order to see the effect of the Reynolds numbers on the change of vortical flow, the velocity distributions, as computed on $50 \times 50 \times 50$ non-uniform grids, are compared against Reynolds numbers in Fig. 4.

Due to space considerations, discussion of results is mainly on the case of $Re = 1000$. In Fig. 5(b), we have plotted the pseudo-streamlines (i.e. sectional streamlines obtained by integrating the velocity components lying in the cut plane) on the $y = 0$ plane, as illustrated in Fig. 5(a). Clearly revealed by this figure is the presence of a pair of counter-rotating vortices with their vortex centers located near the roof corners. From Fig. 5(b), we realize that a planar motion can induce flow motion in the third dimension. Subjected to the rotating disk, with a positive $(+z)$ angular velocity, on the roof of the cavity, fluids in the core of the cavity are mostly lifted up. For fluid particles adjacent to the vertical end wall of the cavity, they move in the downward direction, thus forming a counter-rotating secondary flow structure.

We also plotted in Fig. 5(c) the secondary flow at the diagonal plane shown in Fig. 5(a), revealing the presence of counter-rotating vortices in this plane. It is interesting to find that vortex centroids have drifted towards the core of the cavity. Corner vortices are found at the intersection of the vertical end wall and the floor of the cavity. These corner vortices rotate in a direction opposite to the adjacent secondary flow. The reason for formation of these corner

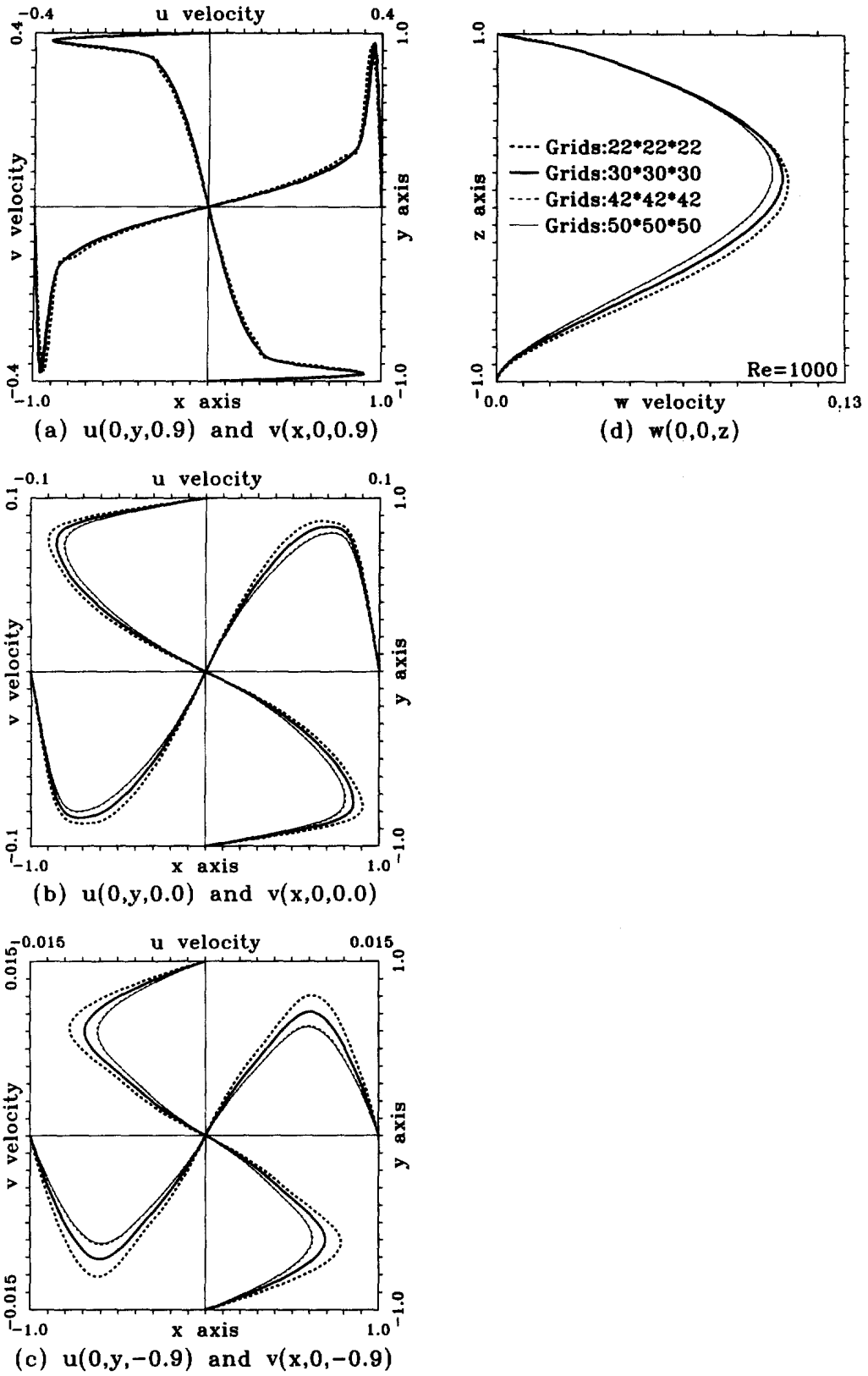

Fig. 3. Grid independence tests for the problem, shown in Fig. 1, with Re = 1000: (a) $u(0, y, 0.9)$ and $v(x, 0, 0.9)$; (b) $u(0, y, 0)$ and $v(0, y, 0)$; (c) $u(0, y, -0.9)$ and $v(0, y, -0.9)$; (d) $w(0, 0, z)$.

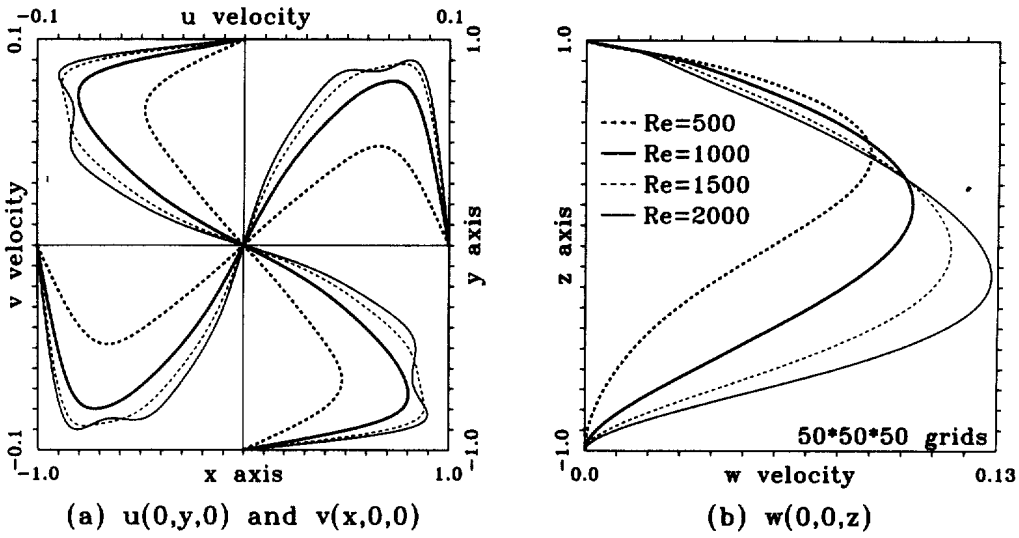

Fig. 4. Changes of velocity against Reynolds numbers for the case conducted on 50 × 50 × 50 meshes: (a) $u(0, y, 0)$ and $v(x, 0, 0)$; (b) $w(0, 0, z)$.

vortices on the diagonal plane is attributed to the fact that fluid flows in corner regions are less affected by the disk rotation. They are instead influenced by the two-dimensional-like lid-driven flow motion. With the vortex center shifted towards the core of the flow and the formation of corner eddies in the lower cavity, the flow pattern resembles the lid-driven cavity flow except at planes $z = 1$ and $r = 0$. For completeness, we also plotted in Fig. 5(d) the pressure contours in the diagonal plane and in the plane ($0 \leq x \leq 1$, $y = 0$, z). The reference pressure is taken as $P_{ref} = 0$ which locates at (0, 0, −1). Fig. 5(d) shows that larger pressure gradient appears in the corner regions near (1, 0, 1) and (−1, −1, 1). As expected, the line where vorticity changes sign coincides well with the sign change of the w-velocity contours shown in Fig. 5(e).

We have also plotted in Fig. 6 the primary flow driven by the rotating disk at planes with different values of z. In planes perpendicular to the rotating axis, in the core of the sectional streamline plots given in Fig. 6(a) resemble a circular rotating flow. In the direction towards the vertical end walls, pressure established along the attached boundary layer poses a resistance force to the circular disk-driven flow pattern. As a consequence, the flow structure in the core is distorted and corner vortices emerge at a plane $z = 0.7$. The presence of the four corners, in turn, aids development of the adverse pressure gradient. As a result, the primary flow tends to decrease its speed near the wall boundary layers. The formulation of secondary flows around four corners should be attributed to the viscous shearing. This explains why singular points are visible in regions contiguous to the four end walls upon which approaching jets impinge. At planes with smaller values of z, their rotation flow patterns are weakened by the fluid viscosity. Such flow patterns on the (x–y) planes differ from the flow pattern just adjacent to the roof where disk rotates. We also plotted in Fig. 6(b) the z-component vorticity contours at different z planes. This figure eludicates the influence of the corner region on the diminishing strength of the vorticity. As Fig. 6(b) shows, near the disk-rotating plane, say at the plane $z = 0.99$, the domain with the positive value of z-component vorticity resembles the shape of rotating disk.

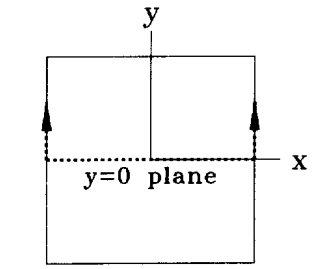

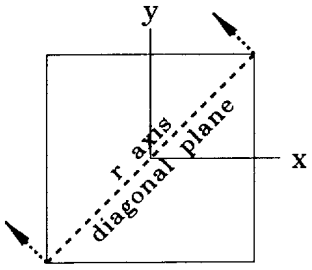

(a) map-indicator

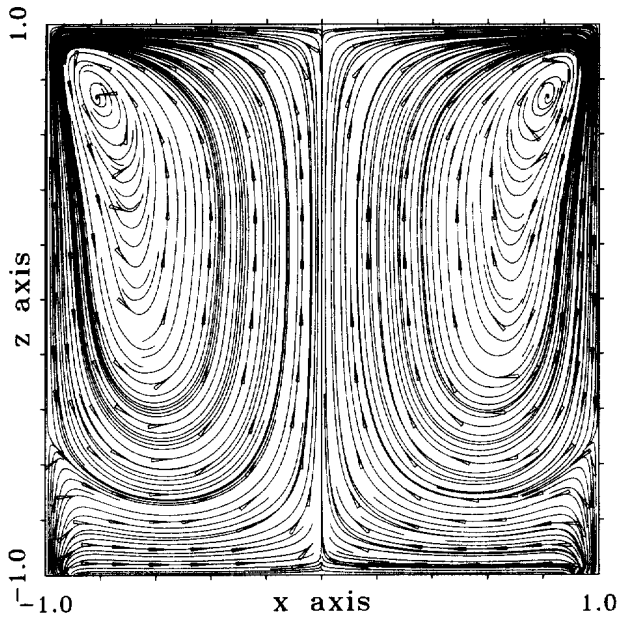

(b) pseudo-streamlines at the y=0 plane

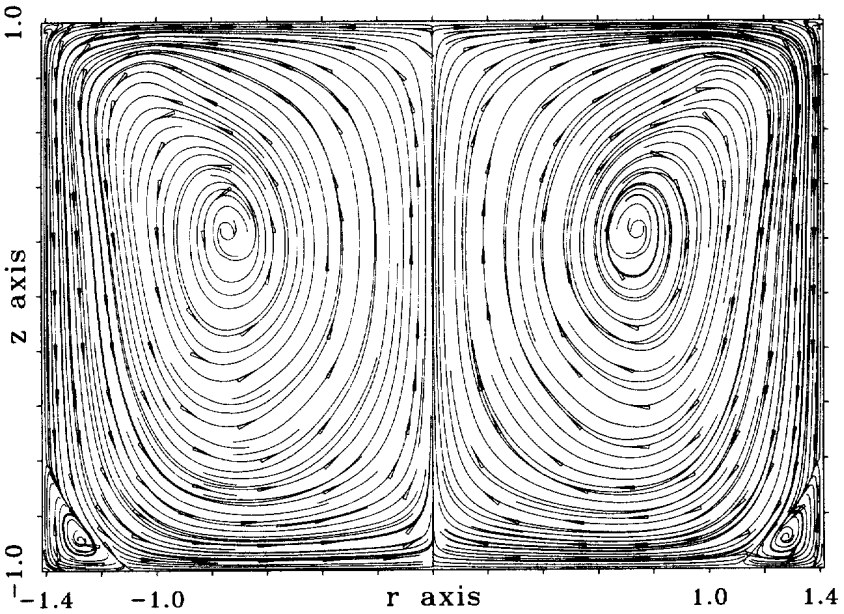

(c) pseudo-streamlines at the diagonal plane

Fig. 5(a–c).

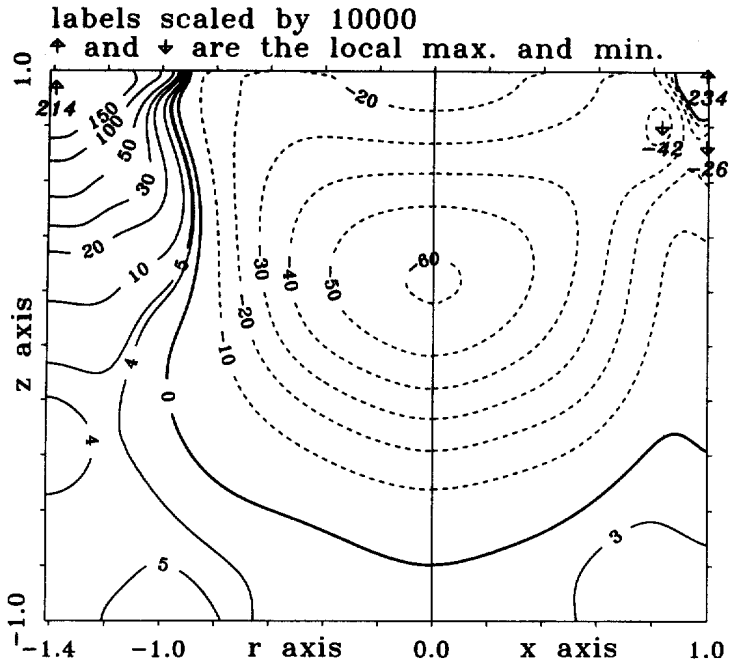

(d) pressure at half of the y=0 and diagonal planes

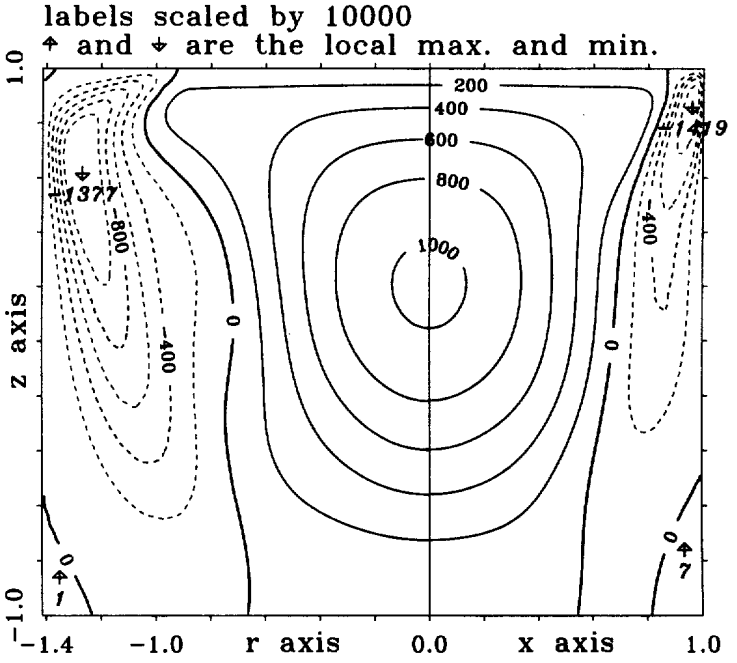

(e) w velocity at half of the y=0 and diagonal planes

Fig. 5. Computed secondary flow structure for the case of $Re = 1000$; (a) illustration of the cutting planes; (b) computed pseudo-streamlines at the $y = 0$ plane; (c) computed pseudo-streamlines at the diagonal plane; (d) pressure contours at half of the $y = 0$ and diagonal planes; (e) w velocity contours at half of the $y = 0$ and diagonal planes

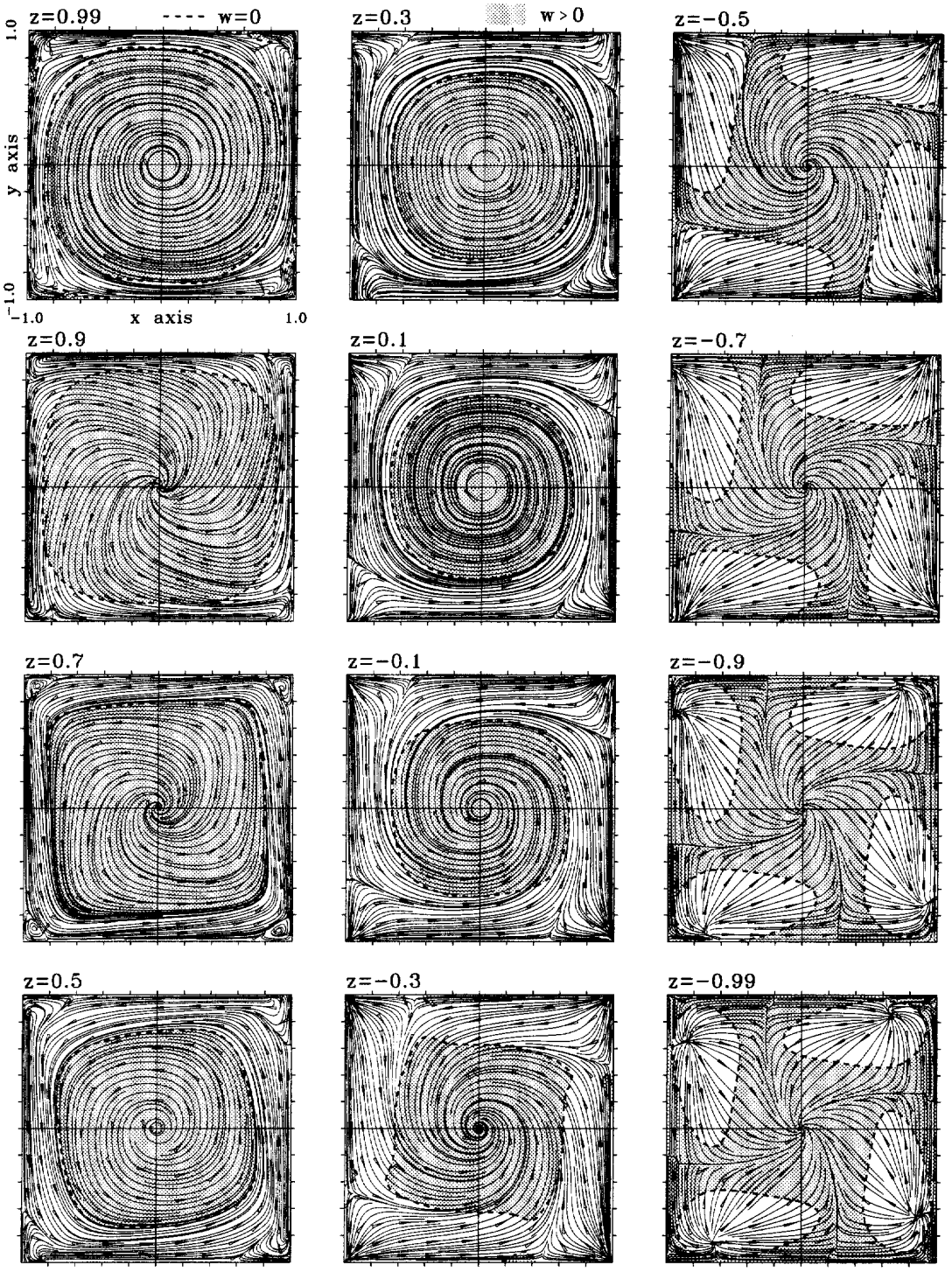

(a) pseudo-streamlines at different z planes

Fig. 6(a).

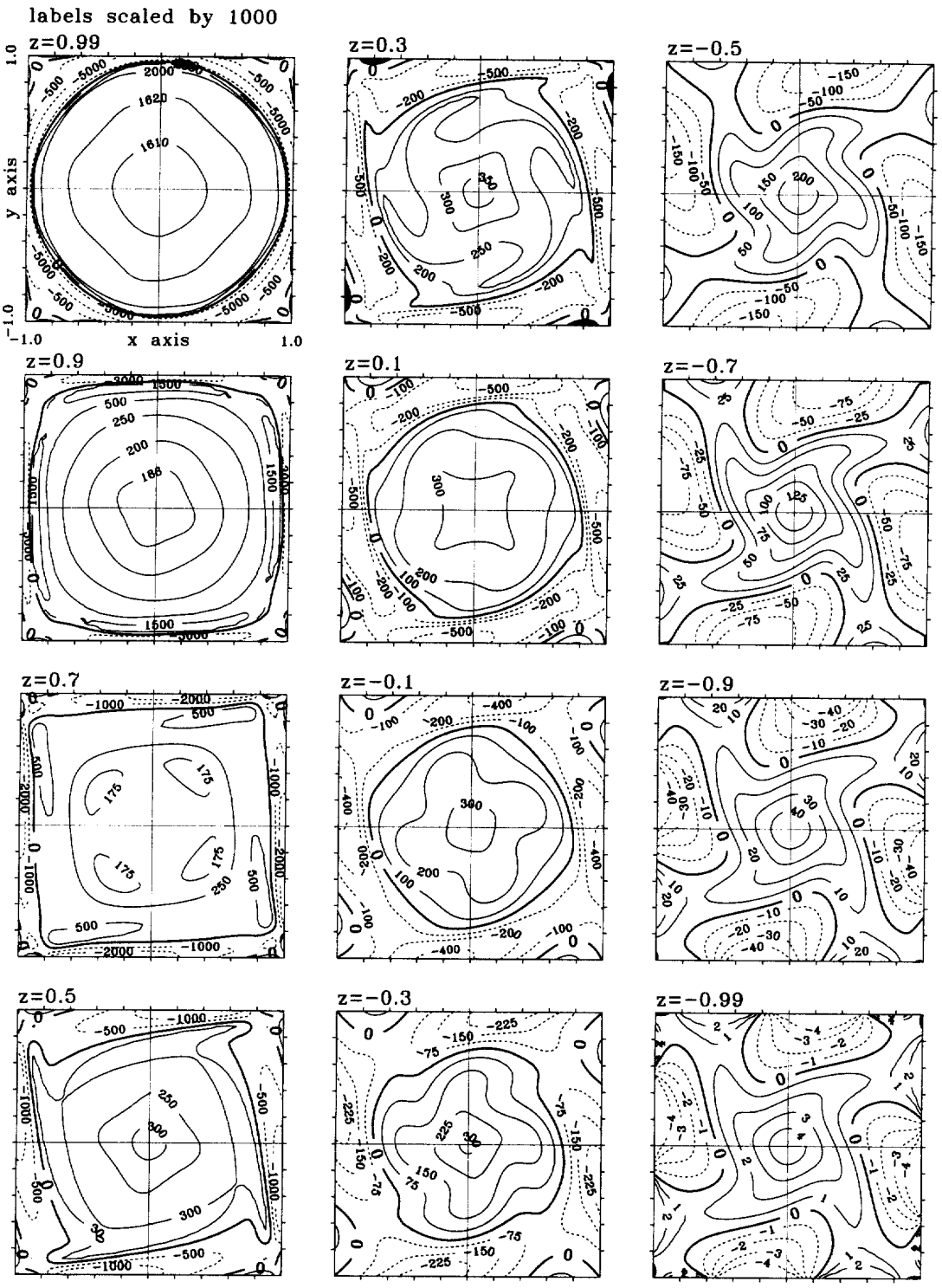

(b) z component vorticity at different z planes

Fig. 6. Computed primary flow structure for the case of Re = 1000 at different z planes: (a) pseudo-streamline plots (The shaded area refers to the area with the positive w velocity component); (b) z-component vorticity plots.

There exists a sharp change of the pressure across the edge of the rotating disk. As noted earlier, lifting force due to the counter-clockwise disk rotation aids the upward-running particle motion for the fluid flow just below the rotating disk. This causes a positive value of w to emerge, as seen in the shaded region of Fig. 6(a). By continuity, the same amount of flows must proceed downwards, leading to a negative value of w elsewhere. This implies the sign-switching of the w velocity component, as illustrated in Fig. 7. As this figure shows, the configuration of $w = 0$ is progressively squared in the downward direction. The contour of $w = 0$ is further distorted by the stagnant corner flow. In the lower half of the cavity, the downward flow ($w < 0$) is only visible in the corner except at planes close to the bottom wall.

By definition, Reynolds numbers increase with the increased disk rotation speed. For this study, we consider $Re = 500$, 1000, 1500 and 2000. Higher rotating speeds correspond to having a higher possibility of lifting particles in the core of the cavity, but has little effect on the transport phenomena along the z-direction. We have studied the general flow patterns against Reynolds numbers and plotted the contours of $w = 0$ and the streamline patterns in the x–y planes in Figs. 8 and 9. From Fig. 8, we are led to know that the flow regime where

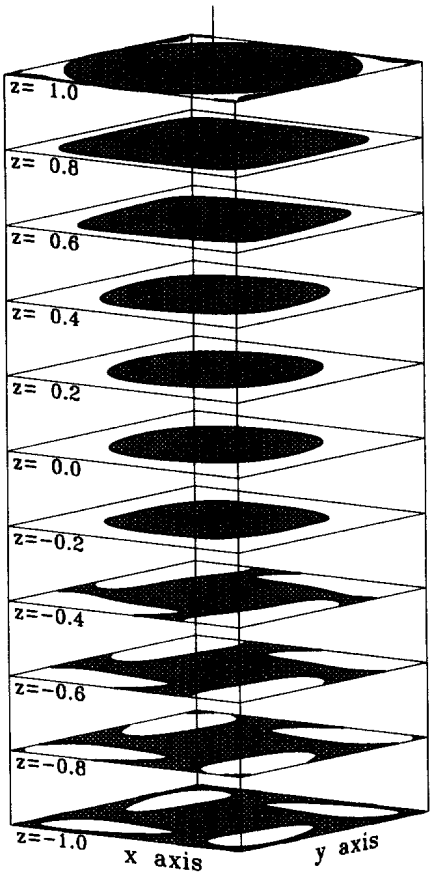

Fig. 7. A three-dimensional plot for showing the positive w velocity component (shaded area) in the cavity which has a disk angular speed ω in the corresponding Reynolds number of 1000.

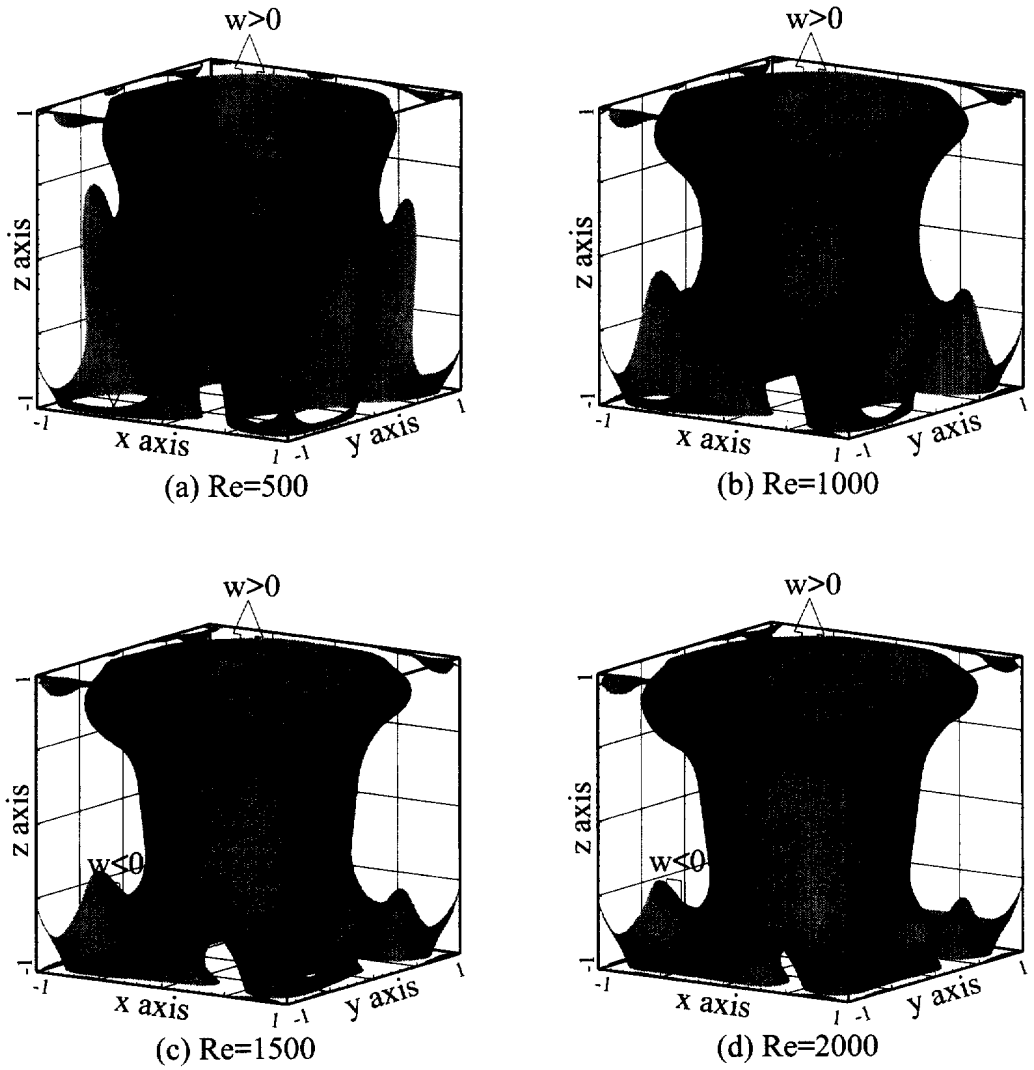

Fig. 8. An illustration of the contour surface of $w = 0$ in the cavity for the cases of: (a) $Re = 500$; (b) $Re = 1000$; (c) $Re = 1500$; (d) $Re = 2000$.

$w > 0$ increases in size near the rotation plane. In the core of the cavity, the area with $w > 0$, on the other hand, becomes increasingly smaller. The higher the Reynolds number is, the larger is the area with $w < 0$ near the floor of the cavity. The primary flow patterns in planes perpendicular to the rotating axis, $+z$, are shown in Fig. 9. For four investigated Reynolds numbers, the streamlines are similar in trend, but differ in their relative values.

4.3. Topological study of vortical flows

We will turn to exploring the kinematically possible disk-driven vortical flow structure. Of possible means to illuminate the flow physics from three-dimensional data, we prefer to adopt

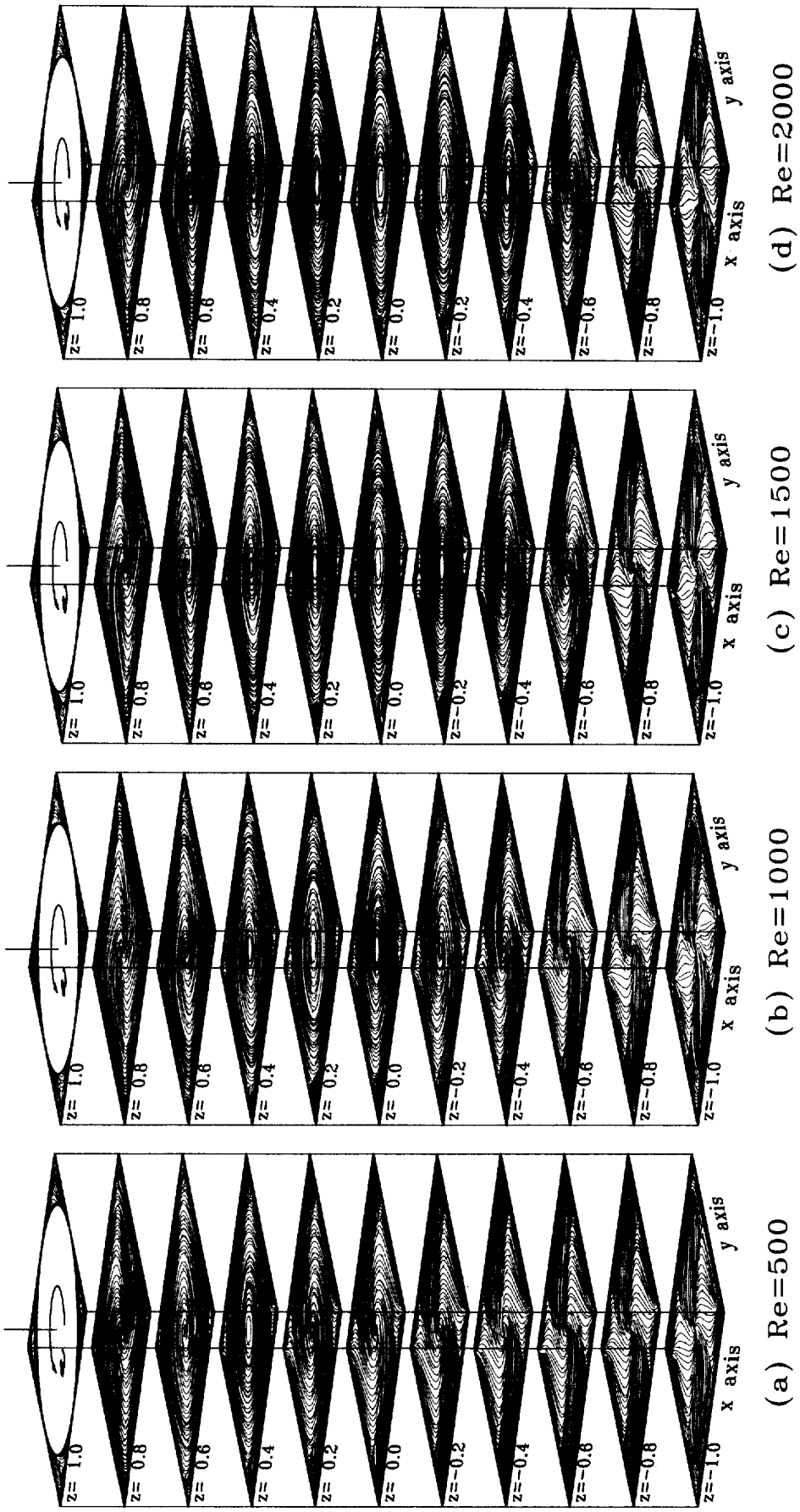

Fig. 9. The computed pseudo-streamlines for the cases with different Reynolds numbers: (a) $Re = 500$; (b) $Re = 1000$; (c) $Re = 1500$; (d) $Re = 2000$.

topology theory [4–7]. For this study, we restrict our attention to study the flow topology via continuous vector fields. Skin-friction lines are chosen for study because the topological pattern of skin-friction lines is mathematically rigorous. Plots of skin-friction lines are regarded as being able to elucidate the flow structure in that flow separation has been defined by the convergence of skin friction lines onto a particular wall streamline that originates from a saddle point. Given that the topology of skin-friction lines corresponds to the experimental surface flow visualization [6], the skin-friction line field can be regarded as the projection of the three-dimensional streamline field onto the body surface. As a result, a topological study of limiting streamlines suffices to determine whether there exist singular points, from which the flow structure can be sketched.

For a given continuous vectors **f**, the value of f_i can be approximated through Taylor series expansion about a critical point **x**(0)

$$f_i = \left(x_j - x_j^{(0)}\right) \frac{\partial f_i}{\partial x_j} + \cdots.$$

We first conduct topological study of fluid flows on the bounded surfaces of the cavity. Limiting streamlines or skin-friction lines are chosen as the content in the vector field **f** discussed above. Depending on the Jacobian, $\partial \mathbf{f}/\partial \mathbf{x}$, singular points can be divided into two main two-dimensional topological classes: nodal and saddle points. Two-dimensional saddles are defined as having one positive and one negative eigenvalue. This implies that the skin-friction vector field points towards the saddle along the negative eigendirection and recedes along the positive eigendirection. Nodal points, attracting or repelling, can be further classified as nodes (regular nodal points) or foci. Nodes are singular points which have two real eigenvalues. We label a critical point as an attracting node if two negative eigenvalues are rendered from the 2×2 Jacobian matrix $\partial \mathbf{f}/\partial \mathbf{x}$. As to the repelling node, its eigenvalues take on the opposite sign of the value. Foci emerge, on the other hand, as the result of complex eigenvalues. Depending on the sign of the real part of the complex conjugate, we assign a repelling focus with positive real eigenvalues, while negative real eigenvalues for an attracting focus. According to the above topological definitions, we plotted in Fig. 10 nodes, spirals as saddles and singular points on the bounded surfaces of the cavity for the case $Re = 1000$. Nodes and spirals in the skin-friction line field are further indicated as being attracting or repelling. Within this classification, a detailed topology pattern of the skin-friction lines is plotted in Fig. 11.

In the interior of the container, the flow topology is better represented by three-dimensional streamlines. Following Legendre [4], a saddle point is defined as a singular point having two eigendirections of the same sign, spanning a plane, and an eigendirection, constituting a line. Around a saddle, streamlines approach/recede from this critical point along a plane and recede from/approach this singular point along a line. Like the two-dimensional topological classification, nodal points are also divided into two sub-classes: regular nodes and spiral saddles. Three-dimensional repelling nodes are associated with three positive real eigenvalues while attraction nodes are those having three negative real eigenvalues. Depending on the sign of the imaginary part of the complex conjugate pair, spiral saddles are referred to as having one real and a pair of complex conjugates.

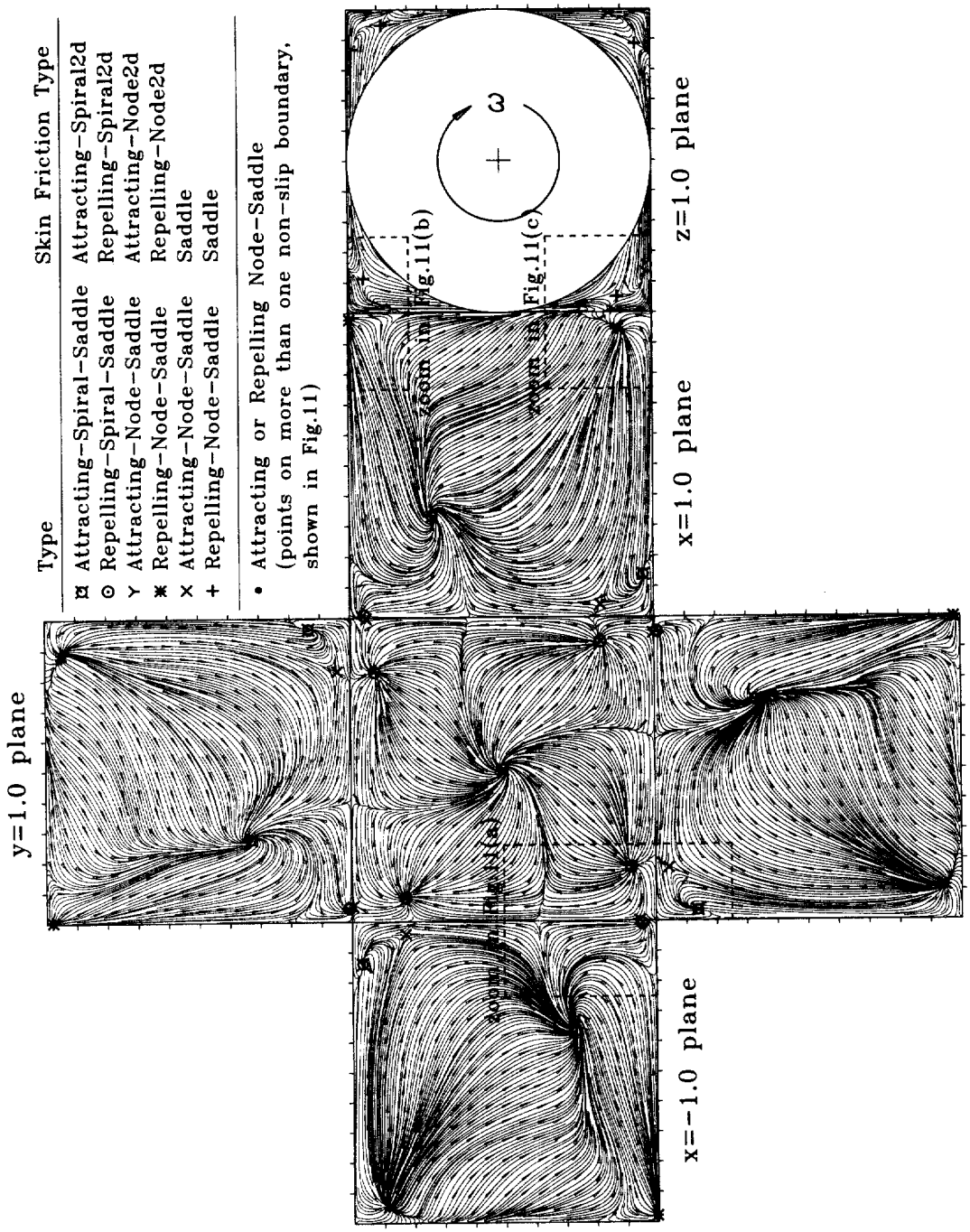

Fig. 10. Illustration of the computed critical points from the limiting streamlines for the case of $Re = 1000$.

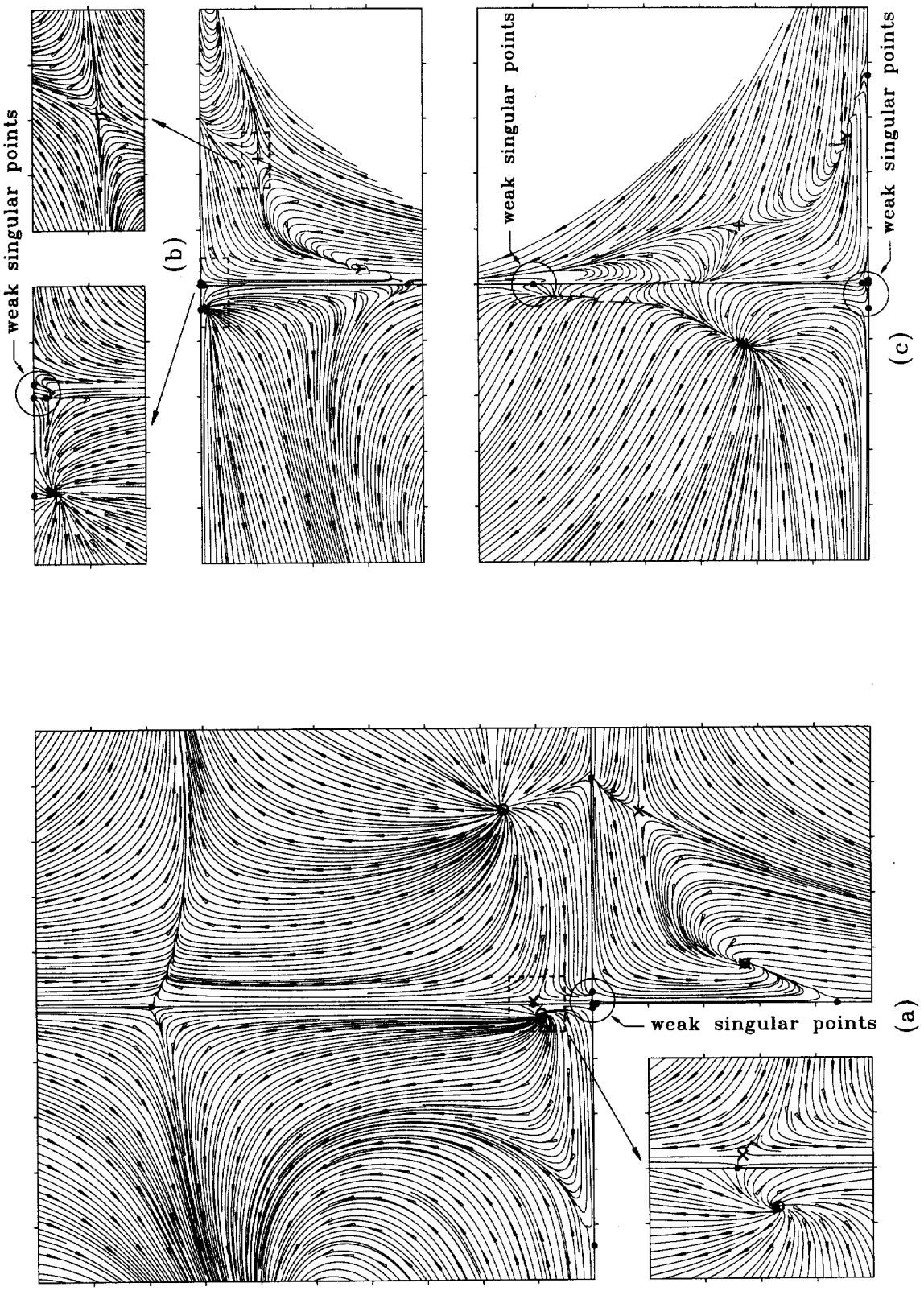

Fig. 11. Detailed flow topologies in the marked area shown in Fig. 10.

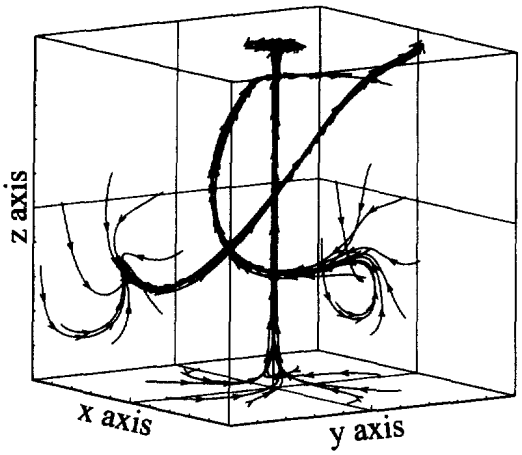

Fig. 12. A three-dimensional plot for showing two different classes of spiral motions of particle tracks for the case of $Re = 1000$.

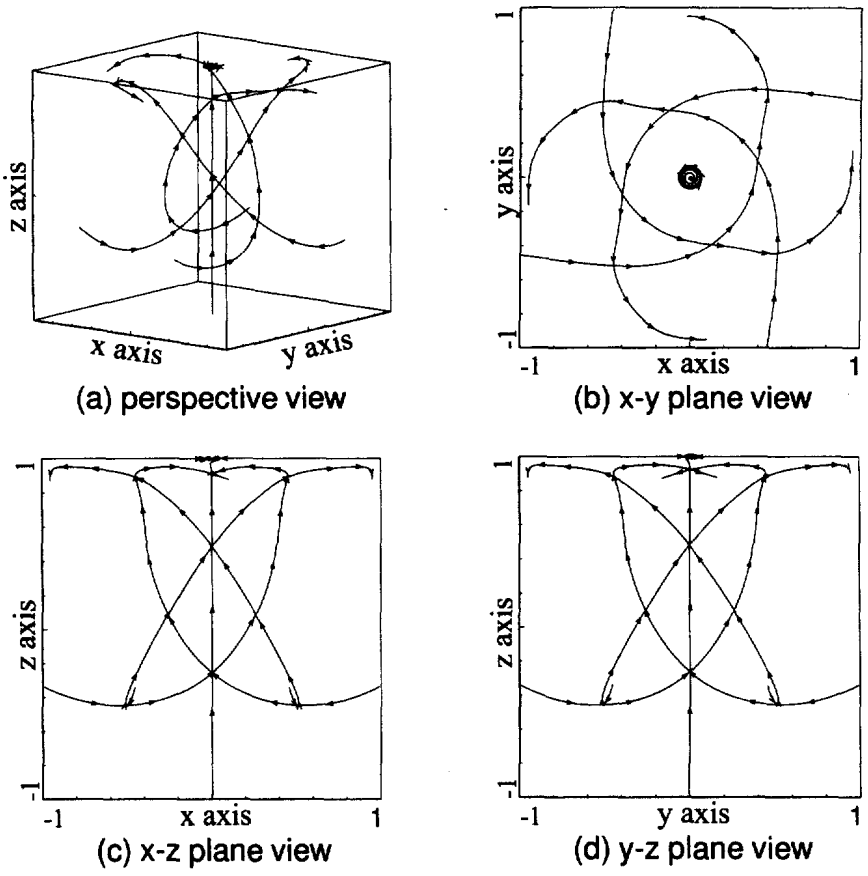

Fig. 13. Different views of particle tracks (or vortex cores): (a) a three-dimensional perspective view; (b) x–y plane view; (c) x–z plane view; (d) y–z plane view.

With the three-dimensional classification of critical points in mind, we plotted in Fig. 12 their particle tracers. In three representative planes just adjacent to $z = -1$, $y = 1$, and $x = -1$, we have placed particles and tracked their trajectories. According to Fig. 12, there

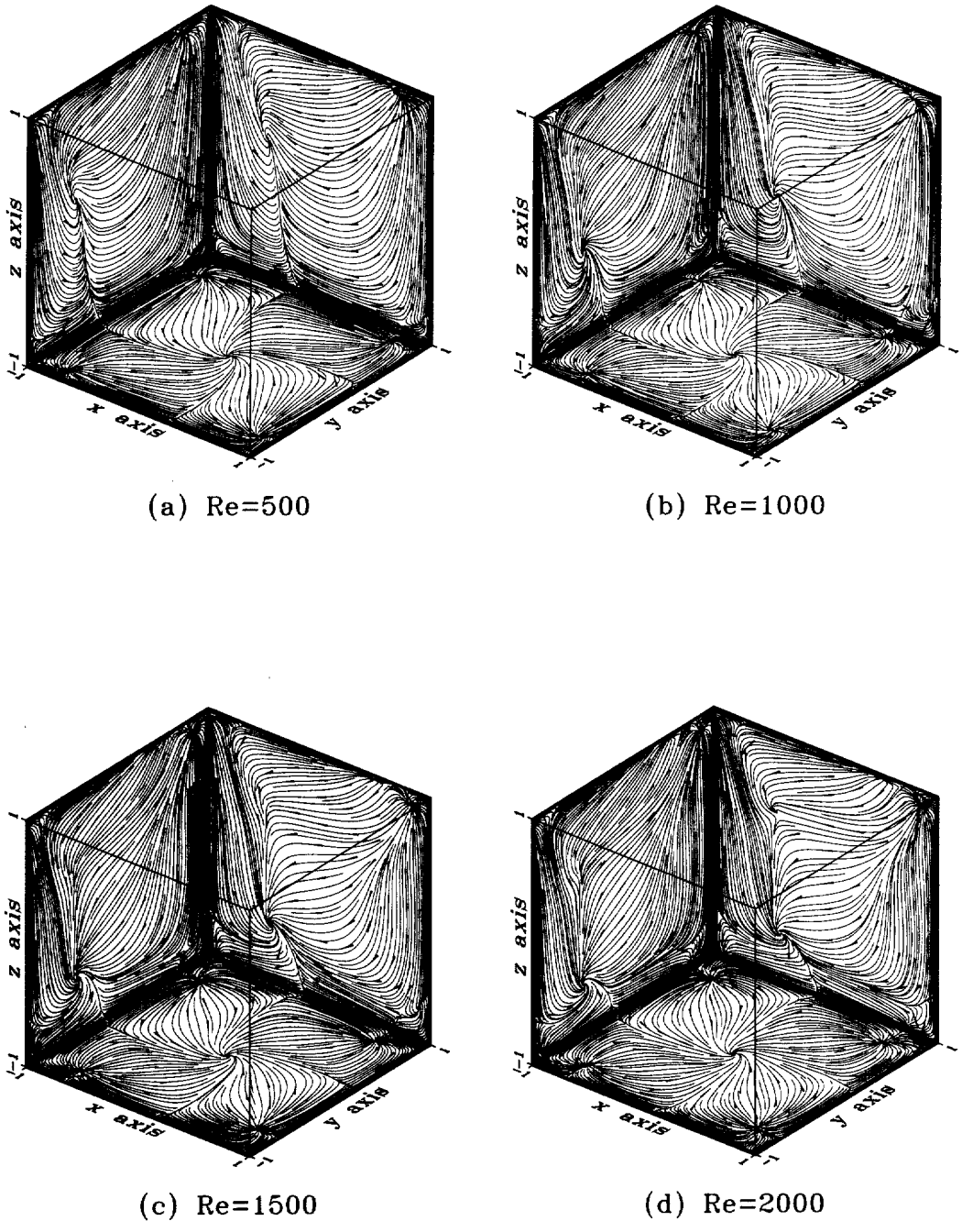

Fig. 14. Computed skin-friction lines for different investigated Reynolds numbers: (a) $Re = 500$; (b) $Re = 1000$; (c) $Re = 1500$; (d) $Re = 2000$.

exist two main types of spiral motions. One group of released particles spirals towards the attracting spiral, say at the $x = -1$ plane, and then proceeds to the upper line along the vortical core line. The other family of particle tracers, released from a plane near the floor of the cavity, is lifted up directly to the roof of the cavity. To provide readers a global picture of the vortical core lines in the cavity, we have plotted a perspective view for them in Fig. 13(a). For clarity, we project these lines on the x–y, x–z, and y–z planes in Fig. 13(b)–(d), respectively. To examine the oil-streak singular point on the bounded surfaces against Reynolds numbers, we have plotted skin-friction lines in Fig. 14. According to these plotted skin-friction lines, the attracting spiral nodes increasingly approach the floor of the cavity as the Reynolds numbers increase. The singular points on the floor of the cavity are, in effect, insensitive to the change of the Reynolds number.

5. Conclusions

Research into the disk-driven vortical flow structure in a cubical cavity has not been reported. Our aim of conducting this study is to explore into the secondary flow structures. With a view to studying three-dimensional kinematically possible flows, we have applied the theory of topology to our discussion of the computed results. Through the mathematically rigorous theory of topology, we are able to sketch the flow structure. We have adopted in this study the skin-friction line field to clarify the oil-streak pattern on the bounded surfaces, while the streamline field to find singular points in the interior of the cavity. Topological changes with Reynolds numbers in the flow structure are also revealed through the calculation of singular points of different portraits.

Acknowledgements

This work was supported by the National Science of Council under Grant NCHC 85-04-004.

References

[1] Ruiz X, Aguiló M, Massons J, Diáz F. Experiments in Fluids 1993;14:333.
[2] Lang E, Sridhar K, Wilson NW. Computational study of disk driven rotating flow in a cylindrical enclosure. J. Fluids Eng. 1994;116:815.
[3] Pao HP. Numerical solution of the Navier–Stokes equations for flows in the disk-cylinder system. Phys. Fluids 1972;15:4.
[4] Legendre R. Séparation de courant l'écoulement laminaire tridimensionel. Rech. Aéro 1956;54:3.
[5] Lighthill MJ. Attachment and separation in three-dimensional flow. In *Laminar Boundary Layers*, II, ed. L. Rosenhead. Oxford University Press, 1963, pp. 26:72–82.
[6] Tobak Murray, Peake DJ. Topology of three-dimensional separated flows. Ann. Rev. Fluid Mech. 1982;14:61.
[7] Yates LA, Chapman GT. Streamlines, vorticity lines and vortices around three-dimensional bodies. AIAA J. 1992;30(7):1819.
[8] Ladyzhenskaya OA. *Mathematical Problems in the Dynamics of a Viscous Incompressible Flow*, Gordon and Breach, New York, 1963.

[9] Chorin AJ. Numerical solutions of the Navier–Stokes equations. Maths Comput. 1968;22:745.
[10] Strikwerda JC. Finite difference methods for the Stokes and Navier–Stokes equations. SIAM J. Sci. Statist. Comput. 1984;5:56.
[11] Rhie CM, Chow WL. *A numerical study of the turbulent flow past on airfoil with trailing edge separation*, Report AIAA-82-0988, 1982.
[12] Abdallah S. Numerical solutions of the pressure Poisson equation with Neumann boundary conditions using a non-staggered grid. J. Comput. Phys. 1987;70:182.
[13] Schneider G, Raw M. Control volume finite element method for heat transfer and fluid flow using collocated variables—1. Computational procedure. Numer. Heat Transfer 1987;11:363.
[14] Harlow FH, Welch JE. Numerical calculation of time-dependent viscous incompressible flow of fluid with free surface. Phys. Fluids 1965;8:2182.
[15] Patankar SV. *Numerical Heat Transfer and Fluid Flow*. McGraw-Hill, New York, 1980.
[16] Leonard BP. A stable and accurate convective modeling procedure based on quadratic upstream interpolation. Comput. Methods Appl. Mech. Engng. 1979;19:59.
[17] Ethier CR, Steinman DA. Exact full 3D Navier–Stokes solutions for benchmarking. Int. J. Numer. Meth. in Fluids 1994;19:369.
[18] Chiang TP, Sheu Tony WH, Tsai SF. Topological flow structure in backward-facing step channels. Comput. Fluids 1997;26(4):321.